Skin-stringer separation in post-buckling of butt-joint stiffened thermoplastic composite panels

van Dooren, K. S.; Tijs, B. H.A.H.; Waleson, J. E.A.; Bisagni, C.

Skin-stringer separation in post-buckling of butt-joint stiffened thermoplastic composite panels

K.S. van Dooren [a], B.H.A.H. Tijs [b,a], J.E.A. Waleson [b], C. Bisagni [a,*]

[a] *Delft University of Technology, Faculty of Aerospace Engineering, Delft, The Netherlands*
[b] *Fokker/GKN Aerospace, Papendrecht, The Netherlands*

ARTICLE INFO

ABSTRACT

Two aeronautical thermoplastic composite stiffened panels are analysed and tested to investigate the buckling behaviour, the skin-stringer separation and the final failure mode. The panels are made of fast crystallising polyetherketoneketone carbon composite, have three stringers with an angled cap on one side, and are joined to the skin by a short-fibre reinforced butt-joint. The panels contain an initial damage in the middle skin-stringer interface representing barely visible impact damage. Finite element analysis using the virtual crack closure technique are conducted before the test to predict the structural behaviour. During the tests, the deformation of the panels is measured by digital image correlation, the damage propagation is recorded by GoPro cameras and the final failure is captured by high speed cameras. The panels show an initial three half-wave buckling shape in each bay, with damage propagation starting shortly after buckling. A combination of relatively stable and unstable damage propagation is observed until final failure, when the middle stringer separates completely and the panels fail in an unstable manner. The test results are compared to the numerical prediction, which shows great agreement for both the buckling and failure behaviour.

1. Introduction

Composite structures are nowadays used in the aeronautical field for primary structures such as wing and fuselage. These primary structures utilise thin-walled designs, consisting of a skin with stiffening elements which can have a wide variety of shapes with open and closed cross-sections. Thin-walled structures are prone to buckle under compression and shear loads and buckling is generally avoided. Allowing primary structures to operate in the post-buckling field below ultimate loads could lead to a significant reduction of weight. This however requires a complete understanding of the structural behaviour in the post-buckling field as it is often seen that failure occurs after buckling [1,2].

This paper considers the experimental test and analysis of two thermoplastic composite stiffened panels, to get a better understanding of the buckling behaviour and skin-stringer separation of thermoplastic panels. This research contributes to the development of thermoplastic composites for aeronautical structures, and to set the next step towards composite structures designed for post-buckling. The combination of different material properties and different manufacturing techniques of thermoplastic composites, compared to thermoset composites, can lead to considerably different structural behaviour. This difference in failure behaviour has been demonstrated in literature mainly at coupon levels,

for example on impact tests [3] and tensile specimens [4]. It is therefore not well known if the analysis methods used for the more classical thermoset composites are applicable for thermoplastic composites, and if the interaction between the buckling and failure behaviour shows similarities.

One of the most common failure modes in the post-buckling field for stiffened panels is skin-stringer separation [5]. Due to the skin out-of-plane displacement caused by buckling, high stresses occur in the interface between the skin and stringer which can lead to separation. Skin-stringer separation is researched mainly on thermoset composite materials, which show a more brittle failure behaviour in comparison to thermoplastic composite materials [6–8].

Orifici et al. [9,10] investigated single-stringer specimens with a blade stringer, both in pristine and damaged configuration with a debond, which showed skin-stringer separation in post-buckling. The pristine panels collapsed when separation started, while the damaged panels exhibited debond growth before collapse. Riccio et al. [11] presented a numerical procedure for skin-stringer separation, which included coupon level tests such as Double Cantilever Beam (DCB) and End Notched Flexure (ENF), and also compared the experimental data of Orifici et al. [9,10] for validation of the single-stringer specimen numerical analysis. The numerical procedure utilised continuum shell

* Corresponding author.
  E-mail address: c.bisagni@tudelft.nl (C. Bisagni).

elements and skin-stringer separation was modelled by the Cohesive Zone Model (CZM), and achieved excellent correlation. The design and analysis of multi-stringer panels with blade stringers was investigated by Degenhardt et al. [12]. The experimental data of this work were later used by Orifici et al. [13] for validation of the numerical prediction for skin-stringer separation in post-buckling. Correlation of the post-buckling behaviour proved to be difficult, due to the influence of geometric imperfections.

Recent work on skin-stringer separation utilises single-stringer specimens with an omega stiffener. Single-Stringer Compression Specimens (SSCS) were designed by Bisagni et al. [14,15], utilising finite element analysis of multi-stringer panels to determine the desired buckling and failure behaviour of the specimens. A total of six SSCS were tested, with and without artificial defects, until collapse. The numerical prediction utilised CZM for skin-stringer separation and a continuum damage model for stiffener crippling and showed good correlation with the tests for both failure modes. The SSCS were further numerically investigated by Vescovini et al. [16], to improve computational efficiency by using a simplified model and introducing a global/local damage analysis. These methods allowed for an efficient parametric study of the effect of structural design and numerical parameters on the buckling, post-buckling and failure behaviour. Dávila and Bisagni [17] presented a combined experimental and numerical investigation for damage tolerance, where numerical analysis were conducted to determine a selection of initial damage sizes and load levels for the fatigue tests. The numerical analysis made use of the Virtual Crack Closure Technique (VCCT) to model skin-stringer separation. Raimondo et al. [18] presented a numerical study utilising the experimental results by Dávila and Bisagni [17], investigating skin-stringer separation due to fatigue using a VCCT based approach. Another method of investigating skin-stringer separation on single-stringer specimens is applying directly the out-of-plane displacement on the skin, as researched by Kootte and Bisagni [19], instead of inducing buckling by longitudinal compression.

The majority of research on thermoplastic composite materials for stiffened structures focuses on the design of the structures, the evaluation of manufacturing processes and the resulting performance [20–22]. More research has been conducted on coupons [23,24] and small elements [25]. The main advantages of thermoplastic materials lay in the high toughness [24], leading to less brittle failure behaviour, the chemical resistance and expanded manufacturing possibilities such as thermoplastic welding [26], hot press forming and co-consolidation processes [27,28]. These manufacturing techniques can result in cost reduction due to a lower number of parts to assemble and out-of-autoclave manufacturing possibilities.

In recent years two projects on thermoplastic aeronautical structures, TAPAS 1 [27] and TAPAS 2 [28], have been successfully conducted in the Netherlands. TAPAS 1 investigated the required manufacturing technology for thermoplastic primary structures, delivered a fuselage shell demonstrator and torsion box demonstrator, which both use the newly developed butt-joint concept. TAPAS 2 considered a thermoplastic orthogrid fuselage shell with new stiffening and joining methods, including the butt-joint concept. This resulted in a fuselage design without fasteners and it shed the need of a so called "mouse hole" in the frame of the fuselage through which the stringer would pass.

The further development of thermoplastic composites for primary structures is explored in the ongoing Clean Sky 2 "SmarT mUlti-fuNctioNal and INtegrated TP fuselaGe" STUNNING project, which focuses on developing the lower half of a thermoplastic multi-functional fuselage demonstrator [29]. Within STUNNING, the performance of thermoplastic composite structures is linked to the manufacturing processes, such as thermoplastic welding and co-consolidation, and a combined experimental and numerical methodology is under development to analyse primary thermoplastic composite structures in post-buckling [30,31].

The thermoplastic stiffened panels investigated in this research have three stringers, with a butt-joint and angled cap. The panels are designed and manufactured by GKN Fokker [32]. The panels include an initial damage in the middle skin-stringer interface, that is representative of Barely Visible Impact Damage (BVID). The buckling and failure behaviour of the panels is analysed by the use of Finite Element (FE) analysis, in which skin-stringer separation is modelled using the VCCT approach [33,34]. The experimental tests make use of Digital Image Correlation (DIC) to capture the deformation field during buckling. Skin-stringer separation is recorded by cameras and panel final failure is captured by the use of two high-speed cameras. The FE analysis and the tests were performed at the Delft University of Technology.

Preliminary analysis results of the first panel were presented by van Dooren et al. [30]. The current study includes the refinement of the analysis of the first panel, the analysis of the second panel and the test campaign.

2. Panel geometry and material

The thermoplastic composite stiffened panels investigated in this work are representative of a business jet fuselage section [32]. The panels have three stringers, with each stringer consisting of a vertical web and an angled side cap, and are joined to the skin with a butt-joint. The panels have two potting tabs, moulded to each end of the panel for load introduction during testing. One of the panels is shown in Fig. 1.

The panels are 495.3 mm long including the potting, 445.3 mm long in between the potting, 344.8 mm in width and the stringer spacing is 152.4 mm, as shown in Fig. 2. The web is 28 mm in height, the cap is 15 mm wide and is angled upwards at 105 degrees w.r.t. the web, as shown in Fig. 3. Short fibre filler material joins the laminates of the stringer and skin, to constitute the so-called butt-joint. The panels have an initial damage in between the bottom of the filler and the top of the skin at the middle stringer, as highlighted by the red area. The initial damage is approximately 70 mm long and is considered a typical damage size to represent BVID for this design. To determine the BVID size, impact tests were performed by GKN Fokker on a larger structure using an indenter with a diameter of $1/2$ inch to obtain an initial indent depth of 1 mm, which is assumed to be at least 0.3 mm after material relaxation [35]. For the larger structure with 15 ply skin, an impact from the inside with a dent depth of 1 mm resulted in a 70 mm crack. Consequently, the initial damage for these three-stringer panels is created by inserting a 40 mm Teflon insert during manufacturing. After manufacturing the damage is extended in a testing machine to a length of approximately 70 mm by applying out-of-plane displacement to the skin. This method creates a sharp crack tip to represent more closely BVID.

The skin is manufactured by advanced fibre placement and the stringer sections consist of pre-forms, which are cut by a waterjet from flat laminates. The stringer sections and filler profiles are assembled in an inner mould and held in place with tooling blocks. The skin is laid on top of the assembled mould with additional glass fibre fabric patches applied on the outer mould side of the skin at the joint locations to improve surface flatness of the skin after manufacturing. The whole section is then vacuum bagged, and co-consolidated in one step in an autoclave. The panels have an additional step purely for test preparation, where epoxy potting is applied to the end of the panels, by placing each end of the panel inside a female rectangular mould which is filled with epoxy.

All the laminated sections are made from Fast Crystallizing PolyEtherKetoneKetone (PEKK-FC) carbon fibre (AS4D) UniDirectional (UD) and are joined by carbon Short Fibre Reinforced Plastic (SFRP) filler PEKK extrusion profiles. The material properties of the AS4D/ PEKK-FC UD and the filler are supplied by GKN Fokker, based on internal characterisation, and are reported in Table 1 and Table 2, respectively. The assumed material properties of the glass fabric PEKK are reported in Table 3. The laminated sections consist of quasi-isotropic layups which are reported in Table 4. The skin has three different layups, named L1, L2 and L3, due to the additional glass fabric plies in the stringer region.

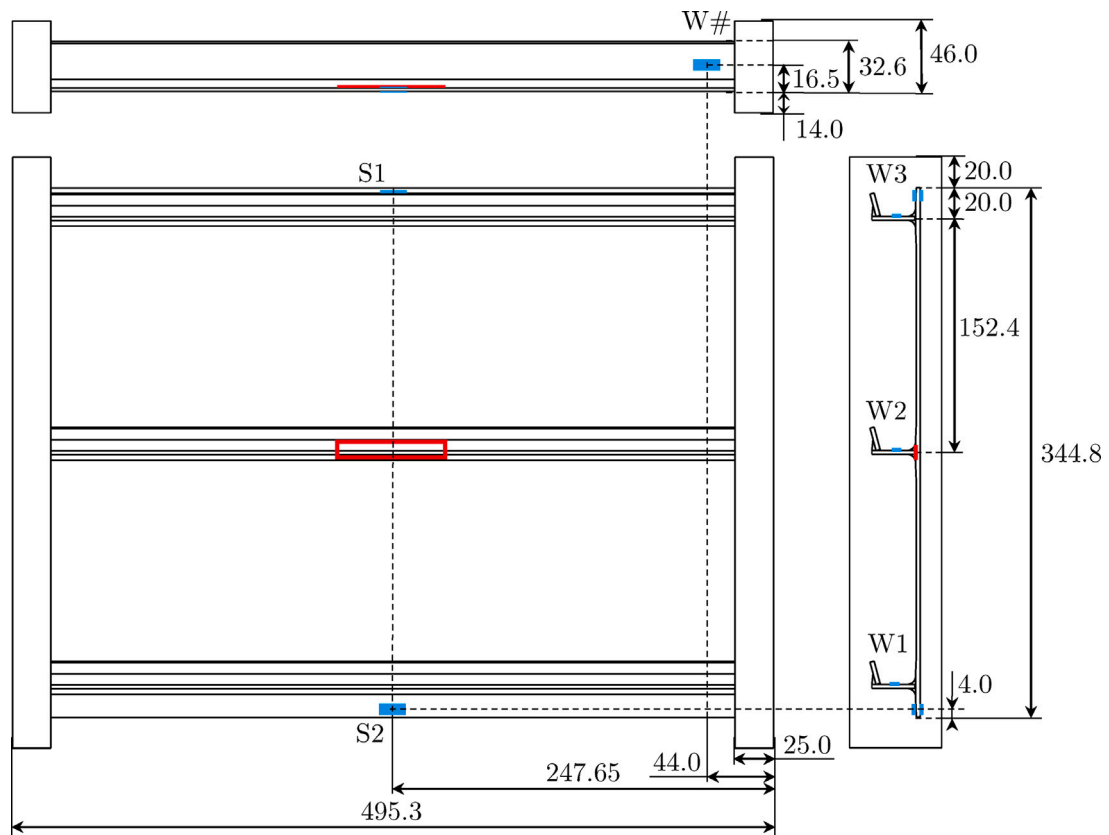Fig. 1. Thermoplastic composite stiffened panel.

Fig. 2. Geometry of thermoplastic composite stiffened panel (dimensions in mm), with initial damage location and strain gauges highlighted in red and blue, respectively.

Table 1
AS4D/PEKK-FC carbon UD ply properties.

E_{11} [MPa]	E_{22} [MPa]	v_{12} [−]	G_{12} [MPa]	ρ [kg/m^3]	t_{ply} [mm]
126100	11200	0.3	5460	1560	0.138

Table 2
PEKK carbon SFRP filler properties.

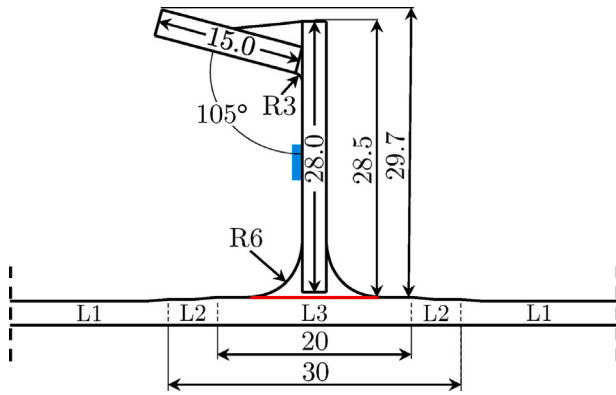| E_{11} [MPa]	$E_{22} = E_{33}$ [MPa]	v_{12} [−]	G_{12} [MPa]	ρ [kg/m^3]
13252	6579	0.42	2389	1560

Fig. 3. Stringer cross-section (dimensions in mm), with initial damage location and strain gauges highlighted in red and blue, respectively.

Table 3
PEKK glass fabric ply properties.

E_{11} [MPa]	E_{22} [MPa]	ν_{12} [−]	G_{12} [MPa]	ρ [kg/m^3]	t_{ply} [mm]
25000	25000	0.3	3000	2200	0.1

Table 4
Layups and total nominal thicknesses of panel sections, with C and G superscript for carbon and glass plies respectively.

Section	Thickness [mm]	Layup
Skin L1	2.484	$[45/-45/0/45/90/-45/45/0/-45]^C s$
Skin L2	2.684	$[0_2]^G[45/-45/0/45/90/-45/45/0/-45]^C s$
Skin L3	2.884	$[0_4]^G[45/-45/0/45/90/-45/45/0/-45]^C s$
Web	2.484	$[45/90/-45/0/45/0/-45/0/\underline{45/-45}]^C s$
Cap	2.760	$[45/90/-45/0/45/0/-45/0/0/\underline{90}]^C s$

3. Geometrical imperfections

Before the tests, the geometrical imperfections of the panels, considered as the deviation with respect to the nominal design, are measured. This allows to determine the effect of the manufacturing process, and to implement the imperfections in the FE model to improve the accuracy of the prediction.

The geometrical imperfections are measured by DIC. The nominal design of the skin is flat, and the geometrical imperfections are therefore measured as the out-of-plane deviation of the skin of the panels with respect to the flat plane. The DIC measurement setup uses two stereo camera and additional lighting, and is shown in Fig. 4.

The measured skin-side imperfections are reported in Fig. 5, where the out-of-plane deviation is projected onto each panel as a contour plot. The measurements show a maximum out-of-plane imperfection of 0.65 and 0.56 mm in outwards direction, and a maximum of 1.55 and 1.08 mm in inwards direction, respectively for the two panels. It is possible to note a slightly V-curved shape in the transverse direction and a slight curvature in the longitudinal direction. The curvature in transverse direction is most likely caused by internal stresses due to the potting curing process and by the mismatch in stiffness of the potting material and composite laminates.

4. Finite element analysis

The buckling behaviour and skin-stringer separation of the two thermoplastic panels is studied, using Abaqus 2019 [36].

The general mesh size is determined by a mesh size sensitivity study. The study starts with linear buckling eigenvalue analysis for a mesh-size ranging from 1.25 mm to 10 mm. This was followed by dynamic implicit analysis for a mesh-size of 1.25 mm and 2.5 mm,

to investigate the buckling and skin-stringer separation behaviour. A mesh-size of 2.5 mm is chosen, as it shows converged results while being computational efficient. The laminated sections consist of continuum shell elements (SC8R). It is chosen to use solid brick elements with incompatible modes (C3D8I) for the filler, which has improved bending behaviour, in combination with wedge elements (C3D6). The solid brick elements (C3D8R) are chosen for the potting material for computational efficiency as this element utilises reduced integration.

The modelling approach makes use of shared nodes to connect the different sections, as shown in the stringer cross-section in Fig. 6. Shared nodes instead of ties shows better computational efficiency and more consistent mesh convergence. The interface between the filler and the skin of the middle stringer is partially bonded by a contact pair definition with VCCT. This area, which is the length of the stringer between the potting, is 445.3 mm long and 9.7 mm wide and has a initial damage of approximately 70 mm in the middle. It is assumed that the pre-crack is present only between the filler and the skin, and that it also only grows in this interface. The possible crack growth into the filler is neglected to lower the complexity of the model. This assumption is based on failure behaviour seen during internal tests by GKN Fokker and three point bending tests by Baran et al. [25]. It is chosen to use VCCT as it shows good results for a relatively course mesh [11,30,33], needed for large structures as in this work, which was also shown by Bertolini et al. [7] in a direct comparison between VCCT and CZM. Furthermore, VCCT requires a pre-crack, and this requirement is automatically fulfilled due to the initial damage in the skin-stringer interface.

The VCCT definition uses the Benzeggagh Kenane (BK) criterion [36, 37] for mixed-mode interface behaviour. The fracture criterion is shown in Eq. (1), which allows a node at the crack-tip to fail when it is equal to or higher than 1. The fracture criteria consists of the critical equivalent strain energy release rate G_{equivC}, defined in Eq. (2), divided by the equivalent strain energy release rate G_{equiv}, given in Eq. (3). The equivalent strain energy release rate is calculated for each node. The parameters in the equation consist of the strain energy release rates for the three different modes, G_I, G_{II} and G_{III}, which are based on nodal displacements and forces.

The critical equivalent strain energy release rate G_{equivC} is calculated using the interface properties G_{IC}, G_{IIC} and G_{IIIC}, which are reported in Table 5. The mode I and II fracture toughness, G_{IC} and G_{IIC}, are based on tests performed by GKN Fokker. The mode III fracture toughness, G_{IIIC}, is assumed to be equal to the mode II fracture toughness. The BK parameter, η, is based on data from literature of a similar material, AS4/PEEK [6].

$$f = \frac{G_{equiv}}{G_{equivC}} \geq 1.0 \tag{1}$$

$$G_{equivC} = G_{IC} + (G_{IIC} - G_{IIIC})\left(\frac{G_{II} + G_{III}}{G_I + G_{II} + G_{III}}\right)^{\eta} \tag{2}$$

$$G_{equiv} = G_I + G_{II} + G_{III} \tag{3}$$

The VCCT definition uses a default fracture tolerance of 0.2 and an unstable crack growth tolerance of 10. This unstable crack growth option is included to improve convergence and computational efficiency when unstable crack growth occurs. The value used for the unstable crack growth tolerance is chosen to limit the amount of nodes released at the same time, and to retain multiple data-points during unstable crack growth. Contact stabilisation is used to stabilise both loss of contact and separation, with a stabilisation factor of 1e-4, which shows improved convergence and computational efficiency. The contact definition utilises node to surface contact discretisation, with the stringer assigned as the master surface and the skin as the slave surface.

The analysis includes first ply failure criteria to determine if material failure could occur in the composite laminates before skin-stringer
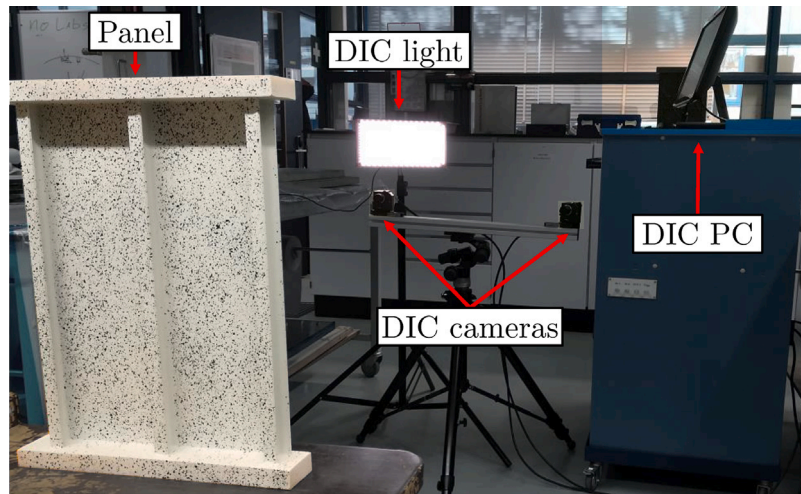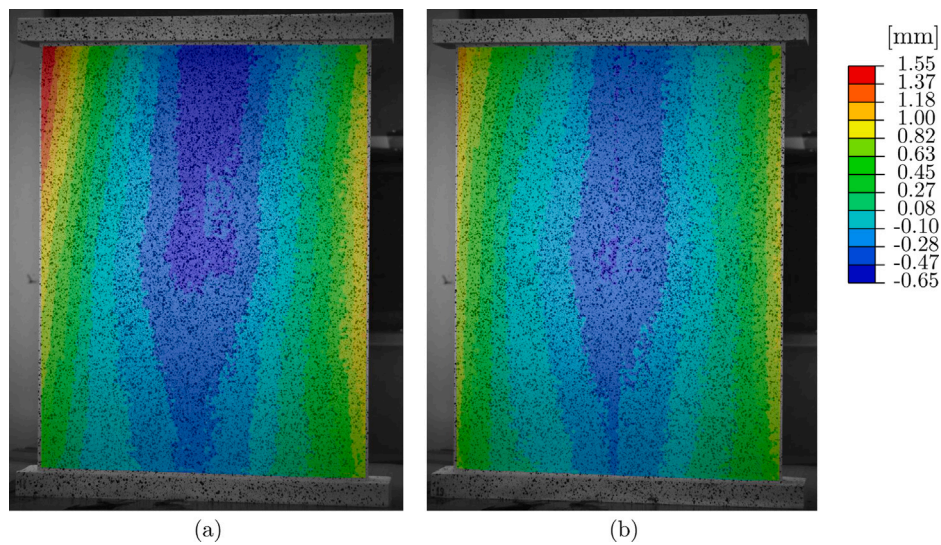
Fig. 4. DIC measurement setup.

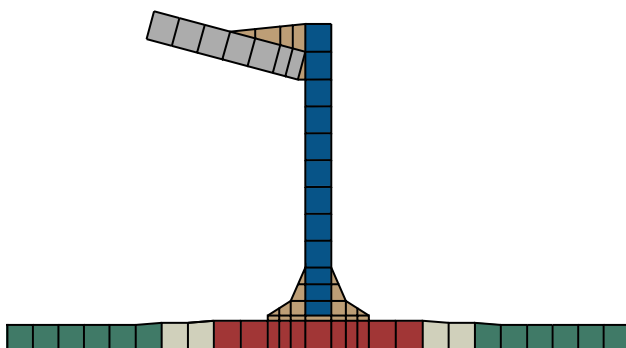**Fig. 5.** Out-of-plane geometrical imperfection of skin-side: (a) panel 1; (b) panel 2.

Fig. 6. FE mesh of the stringer cross-section.

Table 5
Fracture properties of skin-stringer interface.

G_{IC} [kJ/m^2]	G_{IIC} [kJ/m^2]	G_{IIIC} [kJ/m^2]	η [−]
1.41	1.9	1.9	2.3

Table 6
Strength properties of AS4D/PEKK-FC carbon UD ply.

XT [MPa]	XC [MPa]	YT [MPa]	YC [MPa]	SL [MPa]
2559	1575	83.1	284	99

separation. The following criteria are used: Hashin, Tsai–Hill, Tsai–Wu and Max-Stress. The strength properties for input in these criteria are reported in Table 6, and are based on test results by GKN Fokker.

The geometrical imperfections are included in the FE model, as buckling behaviour of thin-walled structures are known to be sensitive to imperfections. Any residual stresses, for example from the manufacturing process, are neglected. The geometrical imperfection are applied to the nominal mesh by means of a FE linear analysis. The out-of-plane coordinates of the DIC imperfection are translated into boundary conditions for the linear analysis using python. This linear
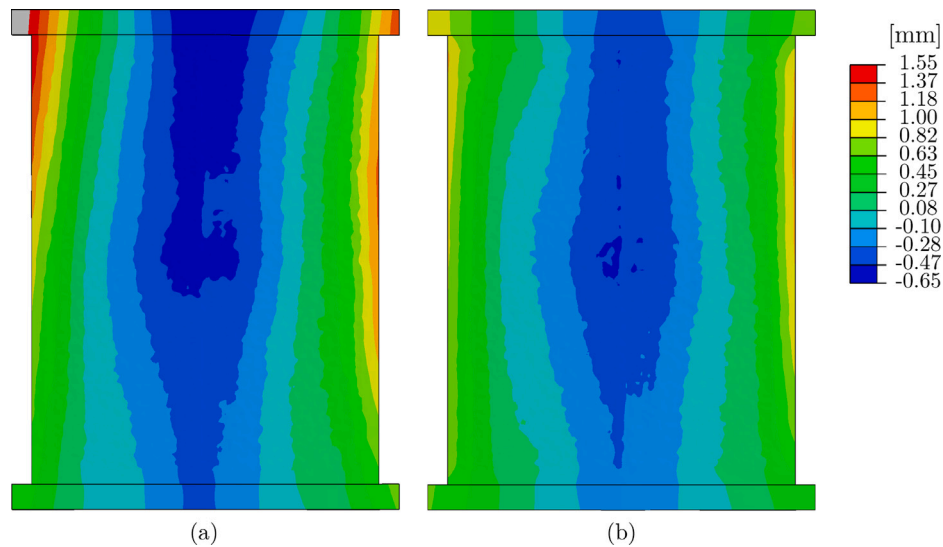
Fig. 7. FE out-of-plane geometrical imperfection of skin-side: (a) panel 1; (b) panel 2.

analysis outputs a nodefile that only includes the deformation field. The nodefile can be used to apply the imperfection in the non-linear analysis, without transferring the stress state of the previous linear analysis. The resulting out-of-plane displacement fields of the linear analysis for both panels, which are the geometrical imperfection used for further analysis, are shown in Fig. 7.

Three types of analysis are performed to determine the structural behaviour of the thermoplastic stiffened panels. Firstly, a linear analysis is used to determine the linear stiffness of the panels, which results in a stiffness of 132 kN/mm. Secondly, a linear buckling eigenvalue analysis is executed to determine the initial buckling shape. The buckling shape is shown in Fig. 8, and consists of three half-waves per bay with the out-of-plane direction of the half-waves anti-symmetric with respect to the middle stringer. The linear buckling load is 100 kN. Thirdly, a dynamic implicit analysis is used to determine the non-linear post-buckling behaviour. The longitudinal compression load-case is applied by displacement boundary conditions. On each end of the panel a reference point is placed. This reference point is connected to each end of the panel (including potting material) by a rigid-body-tie definition. This allows to apply clamped boundary conditions on one end and longitudinal displacement on the other end on only two nodes.

The dynamic implicit analysis includes the contact definition with VCCT for skin-stringer separation with the initial damage of 70 mm, representing BVID. The dynamic implicit step utilises the quasi-static application, which uses the backward Euler operator. The analysis step time is 1 s, with an initial and maximum time increment size of 0.01 s and a minimum of 1e-08 s. The applied displacement is 3 mm, which results in a displacement rate of 3 mm/s. The maximum number of attempts for an increment in the time incrementation controls is increased to 40, to help convergence once separation starts to occur.

5. Test setup

The thermoplastic stiffened panels are tested to study the buckling, the post-buckling behaviour, the skin-stringer separation and the final failure mode using a MTS test machine capable of 3500 kN under compression. Furthermore, the experimental test results and the observed phenomena are used to validate the numerical analysis.

The experimental test setup is shown from the skin-side and stringer-side of the panel in Fig. 9. The panel is placed between the base and the compression plate of the test machine, after which a low preload of 0.5 kN is applied to keep the panel in place. The tests are performed at a loading rate of 0.1 mm/min until final failure of
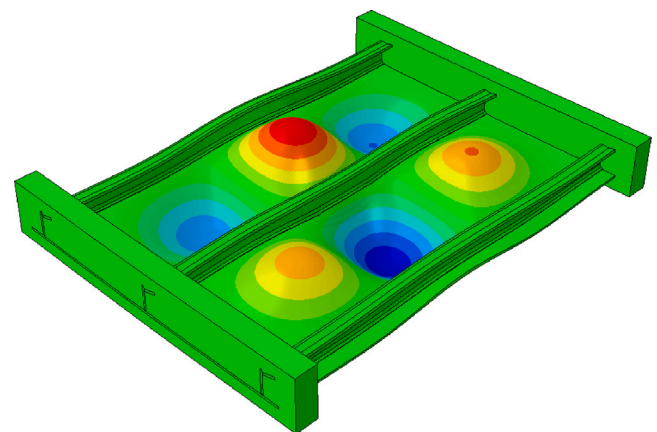

Fig. 8. FE eigenvalue buckling shape.

the panel. The loading automatically stops when the drop in force is measured.

The force and displacement of the compression plate are measured by the load cell and the transducer of the testing machine. Five Linear Variable Differential Transducers (LVDT) are used to measure longitudinal displacement. Two LVDTs are placed on the base plate and three LVDTs are placed on the compression plate. The different locations are chosen to determine if a loading imperfection is occurring. The measured displacements are recorded every 3 s and combined with the force measured by the load cell of the test machine.

A total of 7 strain gauges are attached to each panel to measure strains. A strain gauge is attached to each web under the cap towards the bottom of the panel, while the other strain gauges are attached back-to-back on the free edges of the skin. The locations of the strain gauges are shown in Figs. 2 and 3, with the strain gauges on the web and on the skin named W# and S#, respectively. The locations are chosen according to the results of the numerical predictions, such that the strain gradient is low at each location. The strain gauges on each web show if each stringer is equally loaded in pre-buckling, and how the load distribution changes in post-buckling due to the growth of the skin-stringer separation. The strain gauges on the skin are used to determine loading imperfections due to bending.

Two DIC systems are used to capture the displacement field of both the skin and stringer side of the panels. Each DIC system consists of
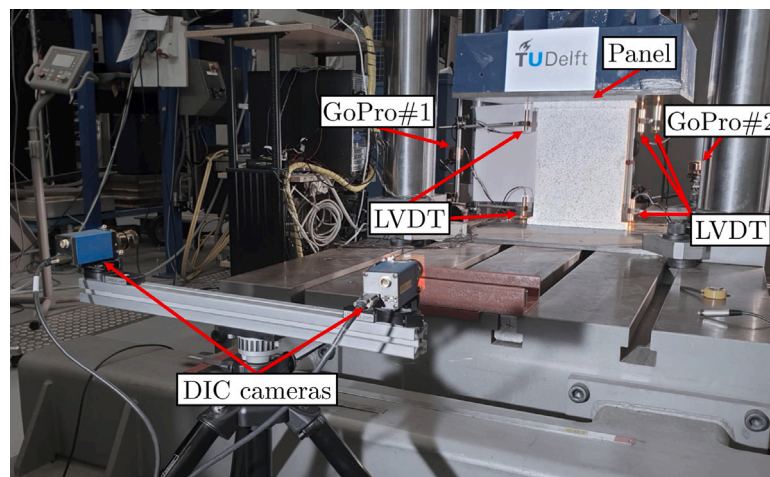
(a)
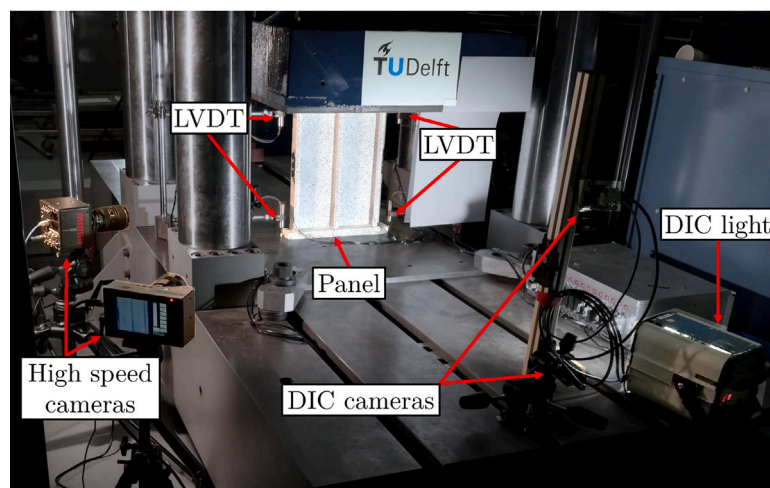
(b)

Fig. 9. Test setup: (a) skin-side; (b) stringer-side.

two stereo cameras and VIC 3D 8 software for post-processing. Each camera is set up to take a picture every 3 s, resulting in approximately 500 pictures per camera. The force measured by the load cell of the test machine is linked to each DIC system to record the corresponding load for each picture. The DIC measurement is used to determine the out-of-plane displacement of the post-buckling shape, and the longitudinal shortening of the panels through the in-plane displacement of the potting.

Three GoPro cameras are used to monitor the test. Two cameras are directed at the initial damage to capture the crack growth behaviour on both sides of the stringer. The third camera is positioned further away to capture the test as a whole.

Two high speed cameras are used to capture the final failure of the panels. Both cameras are focussed on the initial damage at the cap side of the stringer. This side of the stringer is chosen as the numerical predictions show crack growth on this side only. One camera captures a side view of the stringer at 3000 fps, while the second camera is positioned further away to capture the crack growth but also the complete panel at 10,000 fps.

6. Test results and comparison to numerical prediction

This section describes the results of the tests, and compares them to the prediction from the numerical analysis.

6.1. Load versus displacement curves

The load measured from the load cell of the test machine and the longitudinal displacement measured by DIC is used for obtaining the load–displacement curves. The longitudinal displacement by DIC is determined by the difference in displacement from the top and bottom potting. The curves are shown together with the prediction from the numerical analysis in Fig. 10 for panel 1 and 2.

The panels show slight settling behaviour till a load of approximately 20 kN, after which a linear stiffness of 132 kN/mm is measured until buckling occurs at a load of approximately 94 kN for both panels. In the post-buckling field the stiffness is reduced, and continues to be reduced due to a buckling shape change and the growth of the skin-stringer separation. At a load of approximately 145 kN and 187 kN slight drops in stiffness occur for panel 1, while panel 2 shows only one reduction of stiffness at a load of approximately 138 kN. These stiffness reductions are caused by crack growth events, which could also be heard during the test. The panels fail due to skin-stringer separation at a load of 223.0 kN and 215.9 kN for panel 1 and 2, respectively. The difference in load for both the crack growth events and the final failure between the two panels is most likely caused by the difference in the initial damage shape and size and in the geometrical imperfections.

The numerical prediction shows a linear stiffness of 132 kN/mm, followed by buckling at approximately 99 kN. The linear stiffness is
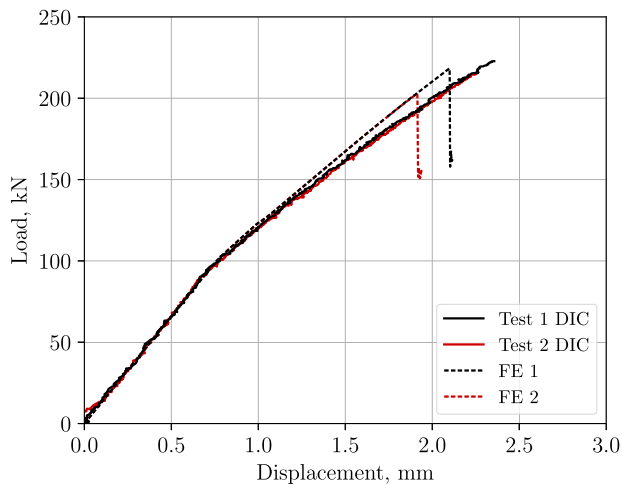
Fig. 10. Load–displacement curves from tests and numerical predictions.

Table 7
Maximum loads from tests and numerical predictions.

	Test [kN]	FE [kN]	Difference [%]
Panel 1	223.0	218.3	−2.1
Panel 2	215.9	202.8	−6.0

predicted accurately and there is a 5.3% over-prediction in buckling load. The loss of stiffness due to crack growth in the post-buckling field can also be seen in the numerical prediction, but the stiffness is less affected in comparison to the test results and is slightly overestimated. The final failure load is predicted to be 218.3 kN and 202.8 kN for panel 1 and 2, respectively, with a difference of 2.1% and 6.0% compared to the tests. The maximum loads measured during the tests and the loads estimated by the analyses are reported in Table 7.

6.2. Load versus strain curves

The strains measured by the strain gauges on the webs of panel 1 are shown in Fig. 11(a). It can be seen that initially the pre-buckling strains in the outside webs are slightly higher compared to the middle web, indicating that there is a small loading imperfection. Then, all three webs show the same stiffness until buckling. In the post-buckling field the strains show a decrease in stiffness. At 145 kN and 187 kN small load drops are seen indicating crack growth events. The strains of the webs of panel 2 are shown in Fig. 11(b). It can be seen that there is more settling compared to panel 1, most likely due to a slightly larger loading imperfection, and there is one load drop indicating a crack growth event at 138 kN.

The numerical predictions capture the load–strain behaviour in the webs well. In the pre-buckling field there is a small difference in the initial settling, as the loading imperfections are not taken into account in the numerical predictions. In post-buckling the strains are slightly over predicted.

The strains in the skin of panel 1 are shown in Figs. 12(a) and 12(b) for location S1 and S2, respectively, with notation IML and OML for inner and outer mould line. At location S1 the measured strains show a small difference between inner and outer mould line indicating a small bending component. At location S2 the influence of bending is more clear, with a larger difference between IML and OML in the post-buckling field. The measured strains at location S1 are considerably higher compared to location S2 in post-buckling. This difference is most likely caused by the non-symmetric stringer, with S1 being located on the opposite side of the cap and S2 being located underneath the cap.

The strains of the skin of panel 2 are shown in Figs. 13(a) and 13(b) for location S1 and S2 respectively. In pre-buckling, location S2 shows a minor bending component, which is not seen for panel 1. This is most likely caused by a small loading imperfection. For both location S1 and S2 the measured strains of panel 2 show more bending compared to panel 1.

The numerical analysis accurately predicts the strain in pre-buckling for both location S1 and S2. A small difference is seen for panel 2 location S2, due to bending in the measured strains in the pre-buckling field. In post-buckling the strains are under predicted at location S1, while the strains at location S2 are accurately predicted for both panel 1 and 2 in post-buckling.

6.3. Out-of-plane displacement

The out-of-plane displacements of the two panels captured by the DIC system are reported in Fig. 14 by contour plots at four load levels, to show the evolution of the deformation in the post-buckling field. For each contour plot the maximum and minimum out-of-plane displacement are reported. A positive sign is for displacement in inwards direction towards the stringer, and a negative sign is for outwards direction away from the stringer. The contour plots for both tests are compared with the results of the numerical analysis.

The test of panel 1 shows an initial three half wave buckling mode, antisymmetric with respect to the middle stringer. At higher loads the buckling shape changes slightly, with a fourth half wave appearing at the top of the right bay. It can be noted that there is a higher inward out-of-plane displacement, in the direction of the stringers, compared to the outward displacement. Initially after buckling it is seen that the magnitude of the out-of-plane displacement is approximately equal in both bays. At higher loads the fourth half-wave becomes more prominent and the magnitude of the displacement becomes higher in the left bay in both inwards and outwards direction compared to the right bay. The half-waves in the left bay are also longer compared to the right bay. This difference becomes more prominent when the fourth half-wave appears in the right bay, and the difference continues to increase until final failure.

The test of panel 2 shows the same three half wave buckling shape as panel 1. In comparison to panel 1, the buckling shape changes with a fourth half-wave at the top of the right bay at a higher load, and the fourth half-wave is smaller in magnitude. The out-of-plane displacement at 116 kN of panel 2 is higher in inwards direction and lower in outwards direction compared to panel 1. This difference might be caused by differences in the geometrical imperfections or loading imperfections, and becomes less at higher loads when the out-of-plane displacements of panel 1 and 2 converge.

The three half-wave buckling shape is accurately predicted, with a great level of similarity in terms of half-wave position and length. The buckling shape change with the fourth half-wave at the top of the right bay is also predicted, but it happens at a higher load compared to what is seen in both tests. The magnitude of the out-of-plane displacements are smaller for inwards direction, while the outwards displacements are initially larger. The outwards out-of-plane displacements at the maximum load is accurately predicted for both panels, indicating that the amount of crack opening due to the outwards displacements might be the dominating factor for final failure.

6.4. Skin-stringer separation

The skin-stringer separation is analysed in more detail with the help of camera footage from the test and the numerical prediction.

On the camera footage of panel 1 a very small tick is heard at 98 kN, while a slightly louder tick can be heard at 120 kN. At 98 kN no crack opening can be seen and the sound seems to origin from the foil for the initial damage being pulled from the skin and chipping paint. When the tick at 120 kN is heard, crack opening is present and it is therefore
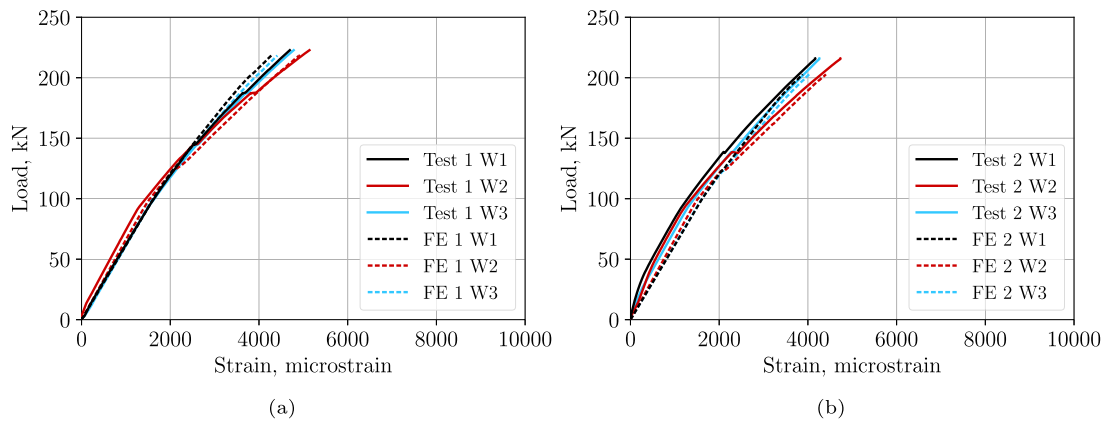
Fig. 11. Experimental and numerically predicted compressive strains in stringer webs: (a) panel 1; (b) panel 2.
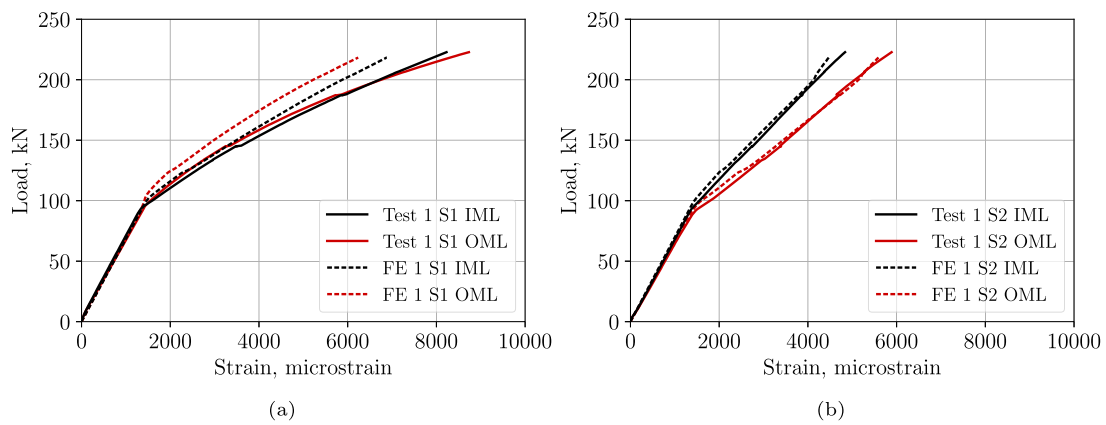

Fig. 12. Experimental and numerically predicted compressive strains of panel 1: (a) S1; (b) S2.
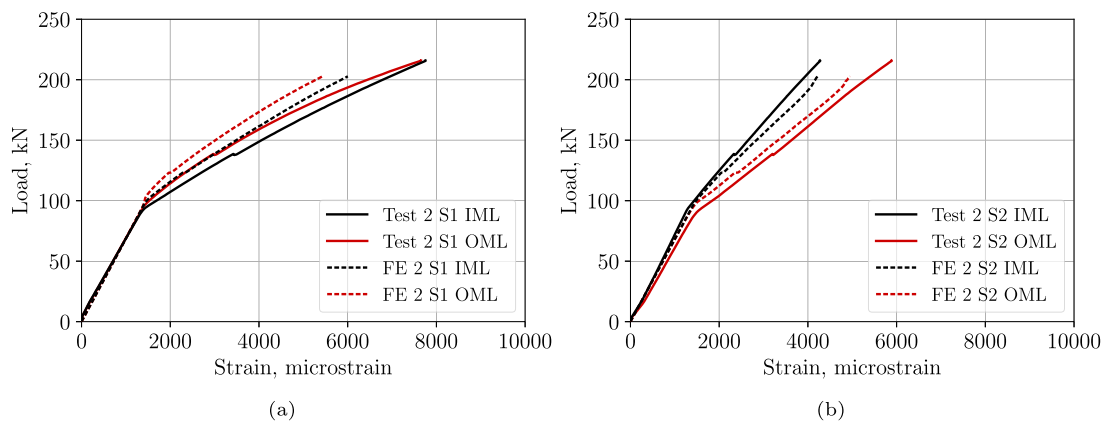

Fig. 13. Experimental and numerically predicted compressive strains of panel 2: (a) S1; (b) S2.

considered the start of the crack growth. On the camera footage of panel 2 a small tick is heard at 119 kN which is considered the start of the crack growth. During the tests of both panels loud ticks can be heard in post-buckling where the initial damage grows initially unstable and then continues with stable crack growth.

As panel 1 and panel 2 show very similar behaviour, only camera footage of panel 1 is here reported. At 156 kN, approximately between buckling and final failure, crack opening can be well distinguished, as shown in Fig. 15. The crack has opened and grown, with more crack

growth in downwards direction compared to upwards direction. The cap-side of panel 1 is shown Fig. 15(c). The opposite side of panel 1, corresponding to the side of the stringer without cap, is shown in Fig. 16, where no crack opening can be seen. The one-sided crack opening is due to the buckling shape, where the outwards half-wave on the cap-side opens the crack, while the inwards half-wave on the opposite side of the cap tends to close it.

The numerical analysis accurately predicts the combination of stable crack growth and crack growth events. The corresponding views are
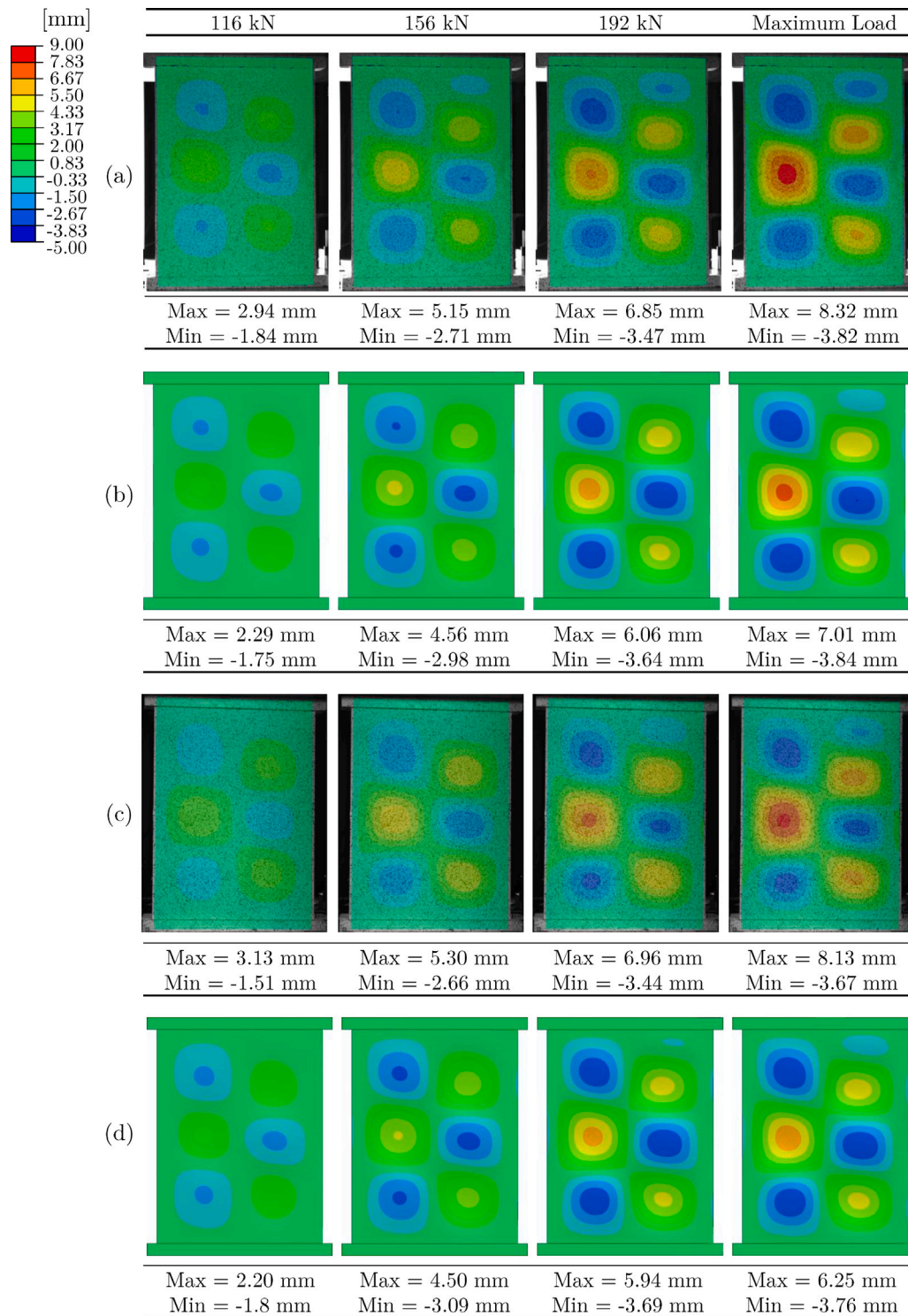
Fig. 14. Out-of-plane displacement: (a) panel 1 test; (b) panel 1 FE; (c) panel 2 test; (d) panel 2 FE.

shown in Figs. 15(a–b) and 16(a–b) for the cap and the opposite side, respectively, for a comparison with the camera footage.

6.5. Fracture surface

To further investigate the skin–stringer separation, the fracture surface is analysed. It is shown over a length of 196.5 mm, as highlighted in Fig. 17(a), which corresponds to the area that is separated before the final failure. The fracture surface of panel 1 is shown in Fig. 17(b),

where the foil inserted in the joint for the initial damage can be noted. The grey marks close to the foil are considered to be caused by the extension process of the initial damage, as the distance between the markings match the initial damage length. Larger grey marks can be seen further away from the foil, with a slight elliptical shape. The shape of these marks is most likely caused by the one-sided crack growth in the post-buckling field.

On the left side there is a delamination of plies from the skin, with only little short-fibre filler material still attached to the skin. On
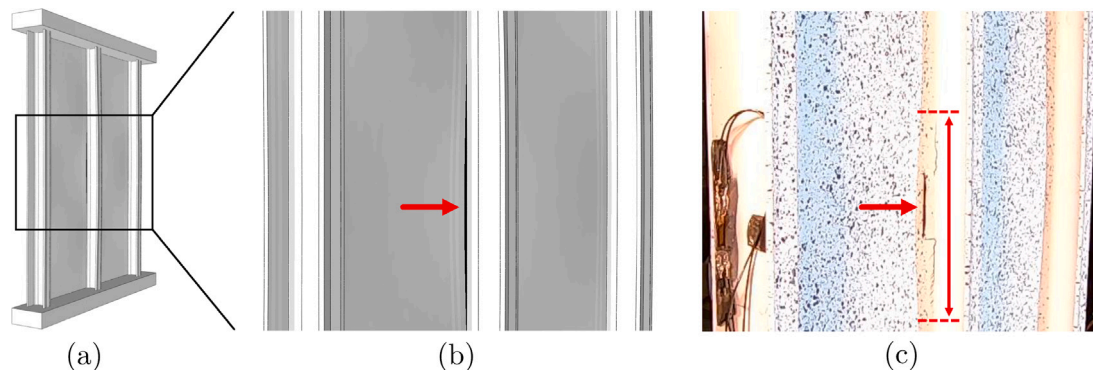
Fig. 15. Crack opening seen from left side of panel 1 at 156 kN: (a) full view of panel; (b) close-up FE; (c) close-up camera footage with visual separation length marked in red.
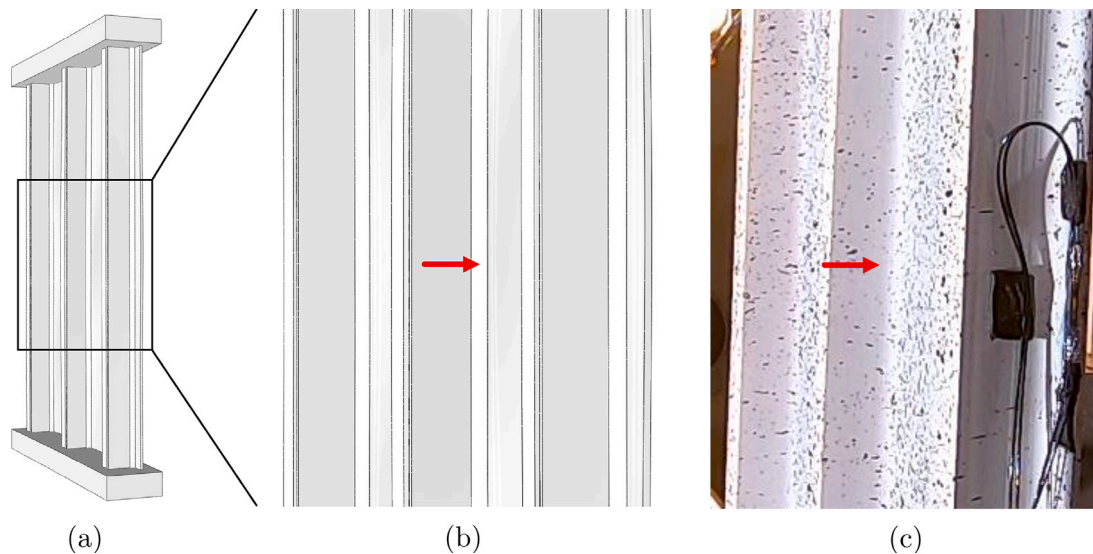

Fig. 16. Closed crack seen from right side of panel 1 at 156 kN: (a) full view of panel; (b) close-up FE; (c) close-up camera footage.

the right side no delamination is seen, and there is more remaining filler material attached to the skin. The remaining filler material is on the opposite side of the stringer, with the cap-side of the stringer showing no remaining filler material. This can be caused by the one-sided crack growth before final failure, followed by the unstable crack growth during final failure where separation also occurs between the web and the filler material.

The fracture surface of panel 2 is shown in Fig. 17(e). The fracture surface is very similar to panel 1, but it shows less grey marks. This might be due to the single unstable crack growth event in post-buckling compared to panel 1. Also, more filler material remains attached to the skin, and delaminations can be seen on both sides of the foil.

The skin-stringer interface of the numerical analysis for panel 1 is shown for the initial damage and at the load of 156 kN in Fig. 17(c) and Fig. 17(d), respectively, where red indicates intact interface, and blue indicates separated interface. The numerical prediction at 156 kN shows a quasi elliptical crack front shape, with a narrow horizontal line of intact interface.

The skin-stringer interface of the numerical analysis for panel 2 for the initial damage and at the load of 156 kN are shown in Fig. 17(f) and Fig. 17(g), respectively. The initial damage is similar to panel 1, but is slightly longer. The interface at 156 kN shows slightly more crack growth compared to panel 1, which might have lead to the lower final failure load of panel 2.

6.6. Mode-mixity

The mode-mixity of the skin-stringer separation obtained from the numerical analysis is investigated, focusing on the results of panel 1 for conciseness as panel 2 shows similar results. The mode-mixity expresses the ratio between peeling (mode I) and shear (mode II/III) loading on the interface. This ratio is of importance as it indicates how the interface is loaded due to buckling, and which type of loading is critical leading to interface failure.

The mode-mixity is determined by using the energy release rates for mode I, II and III as shown in Eq. (4), resulting in a value of 0 for pure mode I and a value of 1 for pure mode II/III. In case of an intact interface, a value of −1 is assigned. The interfaces are analysed over a length of 463 mm, as reported in Fig. 18(a). The mode-mixity of the fracture surface at the start of final failure is shown in Fig. 18(b). The one-sided crack growth before failure is mode I dominated, with final failure being initiated by a narrow line of mode II/III fracture. The fracture surface after the final failure of the panel is shown in Fig. 18(c). The crack growth towards the left is mode I dominated while the crack growth towards the right is mode II/III dominated. The majority of the fracture surface is either dominated by mode I or mode II/III, with only small areas of mixed-mode loading.

$$Mode - Mixity = \frac{G_{II} + G_{III}}{G_I + G_{II} + G_{III}} \tag{4}$$
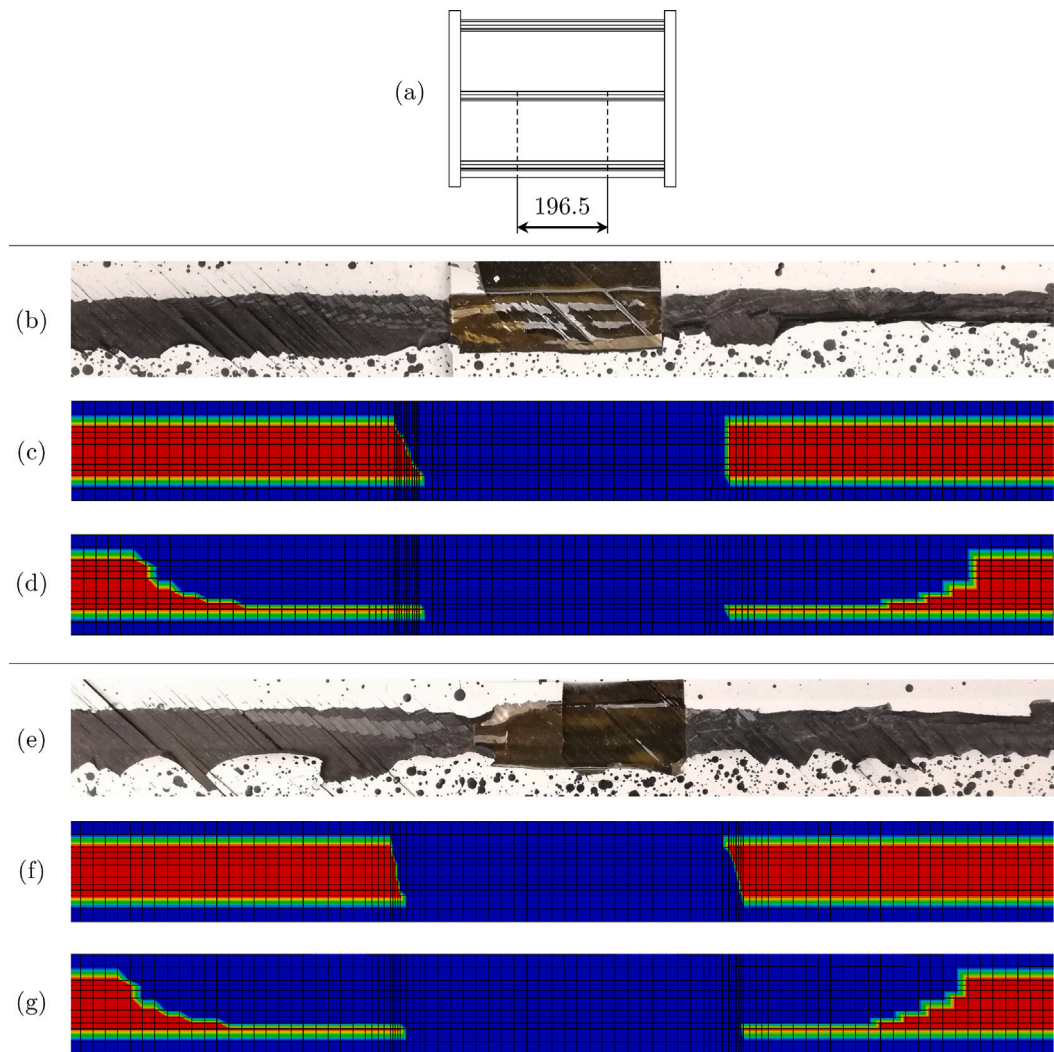
Fig. 17. Top view skin-stringer interface: (a) Interface area of interest; (b) test panel 1 fracture surface; (c) FE panel 1 initial damage; (d) FE panel 1 at 156 kN; (e) test panel 2 fracture surface; (f) FE panel 2 initial damage; (g) FE panel 2 at 156 kN.
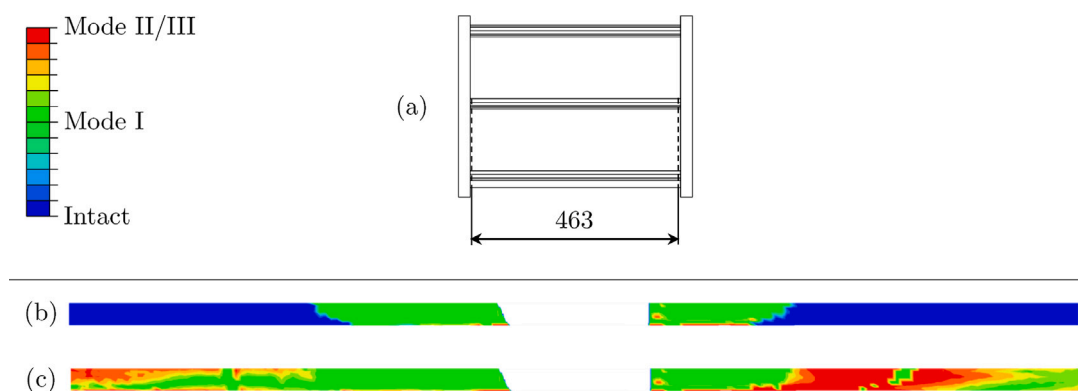

Fig. 18. Panel 1 mode-mixity: (a) Interface area of interest; (b) mode-mixity at start of final failure; (c) mode-mixity after final failure.

6.7. First ply failure

Four first ply failure criteria are included in the numerical analysis to determine if material failure occurs before skin-stringer separation.

The values of the most critical ply for each criterion at the maximum load are reported in Table 8 for both panels. It is possible to see that none of the criteria show first ply failure before final failure, with the Tsai–Wu criterion reporting the highest value for both panels. The most
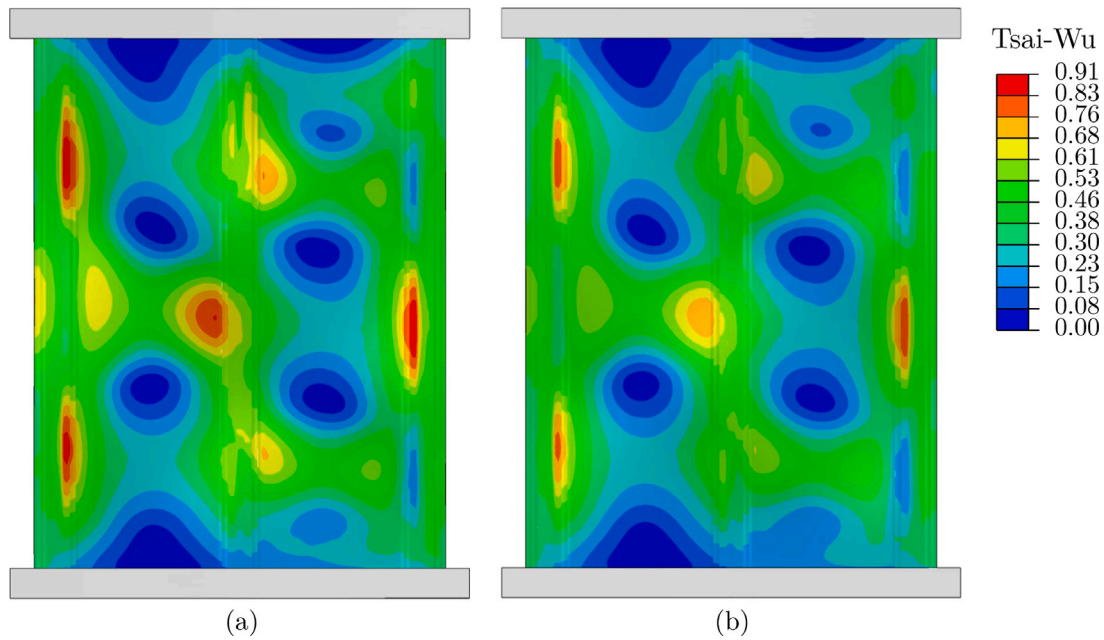
Fig. 19. Tsai–Wu failure criterion of the skin bottom zero ply from the numerical prediction at maximum load: (a) panel 1; (b) panel 2.
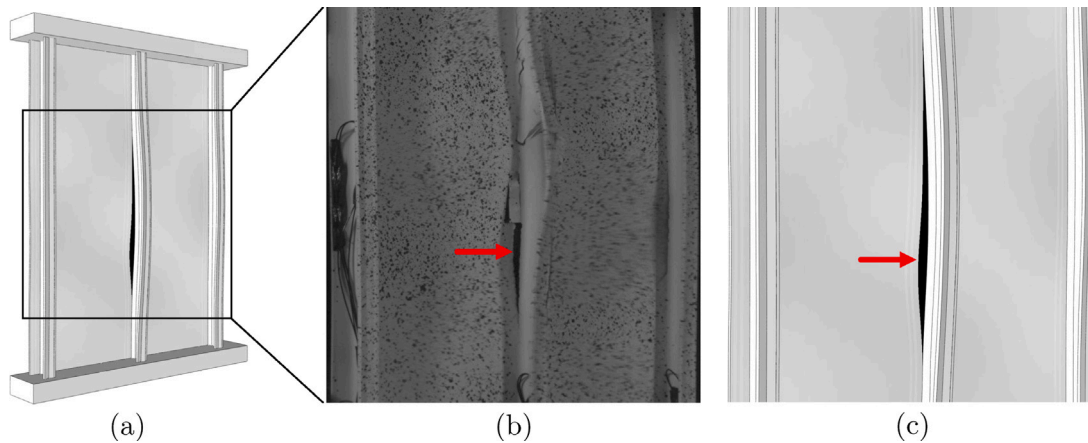

Fig. 20. Crack opening of panel 1 during final failure: (a) full view of panel; (b) high speed camera; (c) close-up FE.

Table 8
Numerical first ply failure criteria values at maximum load.

	Hashin fibre compression	Max stress	Tsai–Hill	Tsai–Wu
Panel 1	0.48	0.72	0.76	0.91
Panel 2	0.37	0.64	0.67	0.82

critical ply according to the Tsai–Wu criterion is the bottom zero ply in the skin, for which the contour plots of both panels are shown in Fig. 19. It can be noted that the most critical locations are underneath the outer stringers, approximately coinciding with the longitudinal location of outwards half-waves of each corresponding bay.

6.8. Final failure mode

The final failure mode is captured by two high speed cameras. The area that is recorded by high speed camera 1 is shown on the FE model in Fig. 20(a). A frame of the 3000 fps high speed footage of panel 1 is shown in Fig. 20(b). It highlights the behaviour during separation of the middle stringer. The crack in the butt-joint grows in downwards

direction and a tunnel forms between two outwards buckling half-waves. Due to the separation of the stringer from the skin, the cap and the web of the stringer also start to show failure, and consequently load carrying capabilities are lost. The numerical prediction of the final failure of the panel is shown in Fig. 20(c). The analysis also reveals crack growth in downwards direction, with a tunnel between two outwards buckling half-waves, similarly to the failure behaviour seen in the tests.

The sequence of the final failure over the full length of panel 2 is captured by the second high speed camera at 10,000 fps, as shown in Fig. 21. Final failure starts with the crack opening (a). Then the crack grows between the web of the middle stringer and the skin (b), after which the separation between the web of the right stringer and the skin occurs (c). This is followed by the separation between cap and web of the middle stringer (d) and failure of the middle cap (e). Then, the web of the left stringer starts to separate from the skin simultaneously with the separation between cap and web of the right stringer (f). This sequence occurs within 2.1 ms, and shows that the skin-stringer separation is the critical failure mode leading to the final failure of the panel.
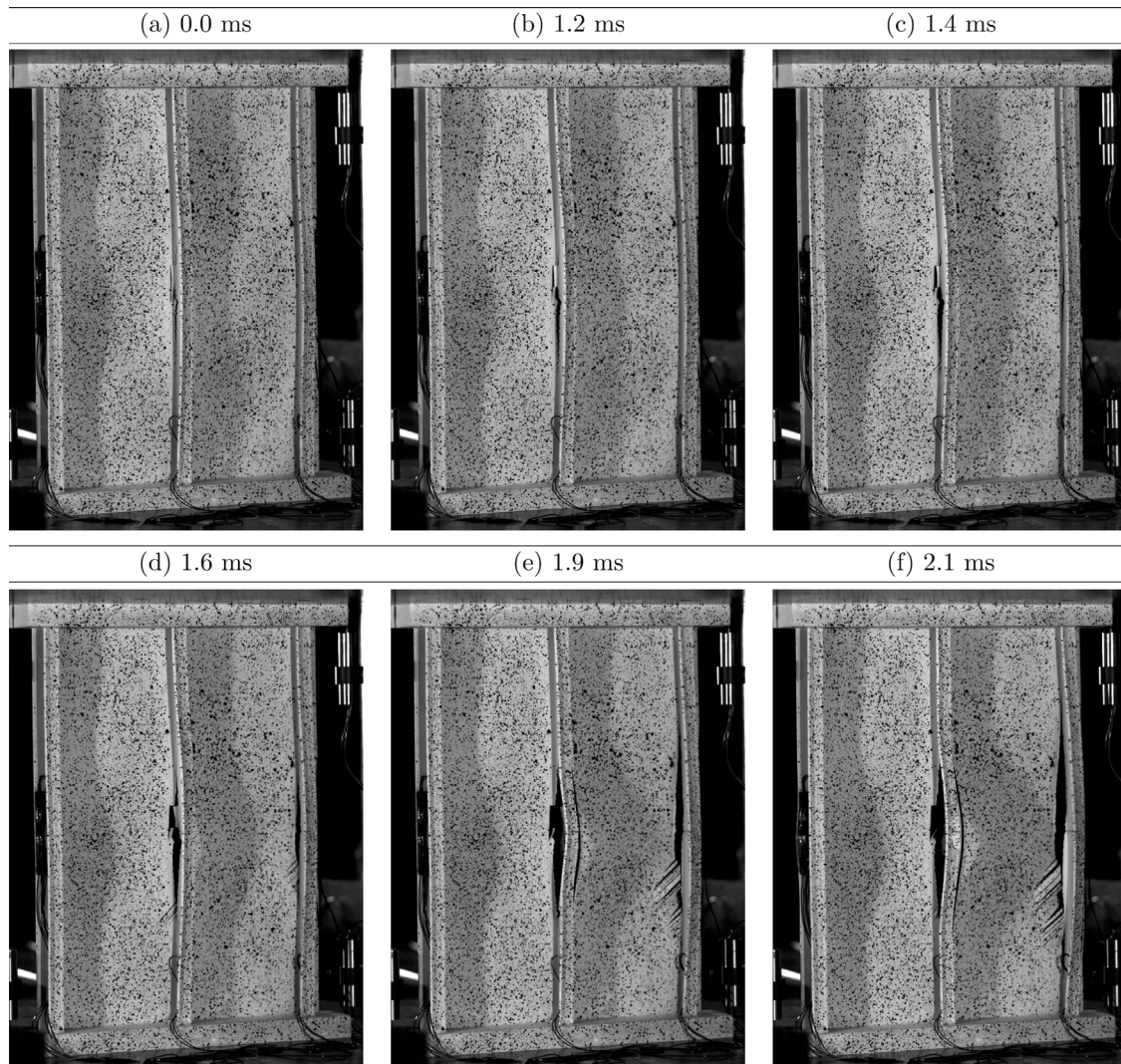
13

Fig. 21. Sequence of final failure of panel 2 captured by high speed camera: (a) crack opening of middle stringer; (b) crack propagation of middle stringer; (c) separation of right stringer; (d) separation of middle cap; (e) failure of middle cap; (f) separation of left stringer and separation of right cap.

7. Conclusions

In this research two butt-joint thermoplastic composite stiffened panels with an initial damage in the skin-stringer interface are successfully analysed and tested. The growth of the initial damage occurs during post-buckling, but only leads to panel final failure at considerably higher loads. The skin-stringer separation is heavily influenced by the buckling shape, as the anti-symmetric buckling shape results in crack opening only on the cap-side of the stringer. The combination of stable and unstable crack growth before final failure can be accounted to both the butt-joint stringer design and the ductile behaviour of the thermoplastic composite material. This structural behaviour is considerably different compared to the more classical designs of the stiffened panels made of thermoset composites.

Numerical analyses are conducted using the commercial finite element software Abaqus. Skin-stringer separation is modelled by the use of the Virtual Crack Closure Technique. The structural behaviour is accurately predicted by the numerical analysis. Even if the post-buckling stiffness is slightly over-predicted after the crack growth events, the analysis has accurately predicted the buckling shape, the post-buckling behaviour, the skin stringer separation and the final failure load and sequence. This shows that the developed methodology is a reliable tool for the design of new thermoplastic aeronautical structures.

CRediT authorship contribution statement

K.S. van Dooren: Conceptualization, Methodology, Software, Validation, Investigation, Visualization, Writing – original draft. **B.H.A.H. Tijs:** Conceptualization, Software, Writing – review & editing. **J.E.A. Waleson:** Conceptualization, Resources, Writing – review & editing. **C. Bisagni:** Conceptualization, Methodology, Resources, Writing – review & editing, Supervision, Project administration.

Declaration of competing interest

The authors declare that they have no known competing financial interests or personal relationships that could have appeared to influence the work reported in this paper.

Data availability

The data that has been used is confidential.

Acknowledgements

This research has partially received funding from the Clean Sky 2 Joint Undertaking (JU), The Netherlands under grant agreement No 945583, STUNNING. The JU receives support from the European Union's Horizon 2020 research and innovation programme and the Clean Sky 2 JU members, The Netherlands other than the Union.

Disclaimer

The results, opinions, conclusions, etc. presented in this work are those of the authors only and do not necessarily represent the position of the JU; the JU is not responsible for any use made of the information contained herein.

References

[1] Bisagni C, Cordisco P. An experimental investigation into the buckling and post-buckling of CFRP shells under combined axial and torsion loading. Compos Struct 2003;60(4):391–402. http://dx.doi.org/10.1016/S0263-8223(03)00024-2.

[2] Falzon BG, Stevens KA, Davies GO. Postbuckling behaviour of a blade-stiffened composite panel loaded in uniaxial compression. Composites A 2000;31:459–68. http://dx.doi.org/10.1016/s1359-835x(99)00085-8.

[3] Vieille B, Casado VM, Bouvet C. About the impact behavior of woven-ply carbon fiber-reinforced thermoplastic- and thermosetting-composites: A comparative study. Compos Struct 2013;101:9–21. http://dx.doi.org/10.1016/j.compstruct.2013.01.025.

[4] Hernandez TPA, Mills AR, Yazdani Nezhad H. Shear driven deformation and damage mechanisms in high-performance carbon fibre-reinforced thermoplastic and toughened thermoset composites subjected to high strain loading. Compos Struct 2021;261:113289. http://dx.doi.org/10.1016/j.compstruct.2020.113289.

[5] Meeks C, Greenhalgh E, Falzon BG. Stiffener debonding mechanisms in post-buckled CFRP aerospace panels. Composites A 2005;36:934–46. http://dx.doi.org/10.1016/j.compositesa.2004.12.003.

[6] Camanho PP, Dávila CG, de Moura MF. Numerical simulation of mixed-mode progressive delamination in composite materials. J Compos Mater 2003;37(16):1415–38. http://dx.doi.org/10.1177/0021998303034505.

[7] Bertolini J, Castanié B, Barrau JJ, Navarro JP. Multi-level experimental and numerical analysis of composite stiffener debonding. Part 1: Non-specific specimen level. Compos Struct 2009;90(4):381–91. http://dx.doi.org/10.1016/j.compstruct.2009.04.001.

[8] Bertolini J, Castanié B, Barrau JJ, Navarro JP, Petiot C. Multi-level experimental and numerical analysis of composite stiffener debonding. Part 2: Element and panel level. Compos Struct 2009;90:392–403. http://dx.doi.org/10.1016/j.compstruct.2009.04.002.

[9] Orifici AC, de Zarate Alberdi IO, Thomson RS, Bayandor J. Compression and post-buckling damage growth and collapse analysis of flat composite stiffened panels. Compos Sci Technol 2008;68:3150–60. http://dx.doi.org/10.1016/j.compscitech.2008.07.017.

[10] Orifici AC, Thomson RS, Herszberg I, Weller T, Degenhardt R, Bayandor J. An analysis methodology for failure in postbuckling skin–stiffener interfaces. Compos Struct 2008;86(1):186–93. http://dx.doi.org/10.1016/j.compstruct.2008.03.023, Fourteenth International Conference on Composite Structures.

[11] Riccio A, Raimondo A, Di Felice G, Scaramuzzino F. A numerical procedure for the simulation of skin–stringer debonding growth in stiffened composite panels. Aerosp Sci Technol 2014;39:307–14. http://dx.doi.org/10.1016/j.ast.2014.10.003.

[12] Degenhardt R, Kling A, Rohwer K, Orifici AC, Thomson RS. Design and analysis of stiffened composite panels including post-buckling and collapse. Comput Struct 2008;86(9):919–29. http://dx.doi.org/10.1016/j.compstruc.2007.04.022, Composites.

[13] Orifici AC, Thomson RS, Degenhardt R, Kling A, Rohwer K, Bayandor J. Degradation investigation in a postbuckling composite stiffened fuselage panel. Compos Struct 2008;82(2):217–24. http://dx.doi.org/10.1016/j.compstruct.2007.01.012.

[14] Bisagni C, Vescovini R, Dávila CG. Single-stringer compression specimen for the assessment of damage tolerance of postbuckled structures. J Aircr 2011;48(2):495–502. http://dx.doi.org/10.2514/1.C031106.

[15] Bisagni C, Dávila CG. Experimental investigation of the postbuckling response and collapse of a single-stringer specimen. Compos Struct 2014;19:493–503. http://dx.doi.org/10.1016/j.compstruct.2013.09.018.

[16] Vescovini R, Dávila CG, Bisagni C. Failure analysis of composite multi-stringer panels using simplified models. Composites B 2013;45:939–51. http://dx.doi.org/10.1016/j.compositesb.2012.07.030.

[17] Dávila CG, Bisagni C. Fatigue life and damage tolerance of postbuckled composite stiffened structures with initial delamination. Compos Struct 2017;161:73–84. http://dx.doi.org/10.1016/j.compstruct.2016.11.033.

[18] Raimondo A, Doesburg SA, Bisagni C. Numerical study of quasi-static and fatigue delamination growth in a post-buckled composite stiffened panel. Compos B 2020;182(2020):107589. http://dx.doi.org/10.1016/j.compositesb.2019.107589.

[19] Kootte LJ, Bisagni C. A methodology to investigate skin-stringer separation in postbuckled composite stiffened panels. In: AIAA SciTech 2020 forum. (2020–0477). 2020, http://dx.doi.org/10.2514/6.2020-0477.

[20] Oliveri V, Zucco G, Peeters D, Clancy G, Telford R, Rouhi M, et al. Design, manufacture and test of an in-situ consolidated thermoplastic variable-stiffness wingbox. AIAA J 2019;57(4):1671–83. http://dx.doi.org/10.2514/1.j057758.

[21] Flanagan M, Doyle A, Doyle K, Ward M, Bizeul M, Canavan R, et al. Comparative manufacture and testing of induction welded and adhesively bonded carbon fibre PEEK stiffened panels. J Thermoplast Compos Mater 2018;32(12):1622–49. http://dx.doi.org/10.1177/0892705718792362.

[22] Peeters D, Clancy G, Oliveri V, O'Higgins R, Jones D, Weaver PM. Concurrent design and manufacture of a thermoplastic composite stiffener. Compos Struct 2019;212:271–80. http://dx.doi.org/10.1016/j.compstruct.2019.01.033.

[23] Vankan WJ, Tijs BHAH, de Jong GJ, de Frel HC, Singh NK. Strength of notched and un-notched thermoplastic composite laminate in biaxial tension and compression. J Compos Mater 2016;50(25):3477–500. http://dx.doi.org/10.1177/0021998315621963.

[24] Tijs B, Abdel-Monsef S, Renart J, Turon A, Bisagni C. Characterization and analysis of the interlaminar behavior of thermoplastic composites considering fiber bridging and R-curve effects. Composites A 2022;162:107101. http://dx.doi.org/10.1016/j.compositesa.2022.107101.

[25] Baran I, Warnet LL, Akkerman R. Assessment of failure and cohesive zone length in co-consolidated hybrid C/PEKK butt joint. Eng Struct 2018;168:420–30. http://dx.doi.org/10.1016/j.engstruct.2018.04.089.

[26] Tijs BHAH, Doldersum MHJ, Turon A, Waleson JEA, Bisagni C. Experimental and numerical evaluation of conduction welded thermoplastic composite joints. Compos Struct 2022;281:114964. http://dx.doi.org/10.1016/j.compstruct.2021.114964.

[27] Offringa A, van Ingen JW, Buitenhuis A. Butt-joined, thermoplastic stiffened-skin concept development. SAMPE J 2012;48(2):7–15.

[28] van Ingen JW. Thermoplastic orthogrid fuselage shell. SAMPE J 2016;52(5):7–15.

[29] Tijs BHAH, van Dooren KS, Bisagni C. Development of a numerical framework for virtual testing to support design of a next generation thermoplastic multifunctional fuselage. In: II European conference on multifunctional structures. 2020, http://dx.doi.org/10.23967/emus.2020.005.

[30] van Dooren KS, Labans E, Tijs BHAH, Waleson JEA, Bisagni C. Analysis and testing of a thermoplastic composite stiffened panel under compression. In: Proceedings of ICCM22 – 22nd international conference on composite materials. (5108–2). 2019.

[31] van Dooren KS, Bisagni C. Design and analysis of thermoplastic welded stiffened panels in post-buckling. In: ASC 36TH annual technical VIRTUAL conference: composites ingenuity taking on challenges in environment-energy-economy. 2021, p. 406–17.

[32] van Ingen JW, Waleson JEA, Offringa A, Chapman M. Double curved thermoplastic orthogrid rear fuselage shell. In: SAMPE Europe conference. Nantes, France. 2019, p. 1–10.

[33] Krueger R. An approach to assess delamination propagation simulation capabilities in commercial finite element codes. In: NASA technical memorandum, NASA/TM-2008-215123. 2008.

[34] Krueger R. A summary of benchmark examples to assess the performance of quasi-static delamination propagation prediction capabilities in finite element codes. J Compos Mater 2014;49:3297–316. http://dx.doi.org/10.1177/0021998314561812.

[35] Fualdes C. Composites@Airbus. Damage tolerance philosophy. FAA workshop for composite damage tolerance and maintenance, July 19-21, 2006. 2016.

[36] Abaqus 2019 documentation. Dassault Systemes Simulia Corp. 2019.

[37] Benzeggagh ML, Kenane M. Measurement of mixed-mode delamination fracture toughness of unidirectional glass/epoxy composites with mixed-mode bending apparatus. Compos Sci Technol 1996;56:439–49. http://dx.doi.org/10.1016/0266-3538(96)00005-x.